Electrokinetic Fluidic Dielectrophoresis for Precise On-Chip Fluidic Routing

By

Edwin Lavi

A thesis submitted to Johns Hopkins University in conformity with the requirements for the degree of Master of Science in Engineering

Baltimore, MD

May, 2018

Abstract

Recent developments in the field of microelectromechanical systems (MEMS) enable access to small low-cost precision analytical tools for use in biological, pharmaceutical, energy and space industries. In this thesis, we demonstrate a new method to control microfluidic fluid flows and analyte concentrations using on-chip solid-state electrokinetic switches. In particular, we demonstrate the ability to dynamically control spatial chemical concentration gradients for potential applications in studying biased cell motility during cellular chemotaxis. This work is an important development because it will enable the rapid and dynamic control of microfluidic concentration profiles which can be leveraged to better elucidate chemotactic features of motile cells. Currently, the most established chemotaxis assays are chamber and needle assays. These methods produce concentration gradients using passive chemical diffusion using a quasi-steady source of chemokine concentration. As such, it is difficult and time consuming to dynamically control these gradients during cell migration experiments. The goal of this thesis project is to integrate electrokinetics to enable a new class of precision and control of chemical gradients for directed cell migration studies on a single-cell level.

In this paper, we leverage an electrokinetic phenomena, fluidic dielectrophoresis (fDEP) which occurs at liquid-liquid electrical interfaces that have been subjected to orthogonal externally applied electric fields. This field polarizes the fluid interface and produces an electrohydrodynamic stress and net fluidic motion, or displacement, in the direction perpendicular to the fluid flow. Here we present work that extends fDEP's usefulness to applications for microfluidic fluid routing and mixing. Using pressure driven flow we create two different fluidic interfaces. Each interface is driven over an array of metal electrodes fabricated on the surface of a microchannel. By applying an alternating current (AC) electric field across an electrode array, fluid is controllably deflected across the interface. To create each electrical fluidic interface, we used two different electrolytes – one fluid possesses a greater electrical conductivity and the other has a greater dielectric constant. At low frequencies below the timescale for conductive polarization, the high conductive stream deflects into the low conductive stream. Whereas above this timescale at high frequency, the high dielectric stream is deflected into the low dielectric stream. Based on the difference in electrical conductivity and dielectric constant of the two fluids, we observe frequency and voltage dependent changes in both magnitude and direction of the deflected stream.

Using this Maxwell-Wagner polarization behavior, we developed new microfluidic/electrokinetic devices for controlling the chemical concentrations in physiological cell buffers. In particular, we characterized fDEP for use in controlling and studying the chemotaxis of the social amoebae, *Dictyostelium discoideum*. When starved or depleted of a food source, these cells undergo a development

cycle in which they become sensitive to and migrate up concentrations of the chemokine, cyclic adenosine monophosphate (cAMP). We created an electrical interface using two conductive cell buffers with the equal dielectric constants and disparaging electrical conductivities. One buffer stream was loaded with a fixed and known concentration of cAMP. We show that by adding a chemoattractant, namely, cAMP to the high conductive buffer the magnitude and direction of the cAMP gradient can be controlled. We observe a similar voltage and frequency effects as seen in previous fDEP works where at low frequencies, the high conductive stream, is deflected into the low conductive stream. Furthermore, by altering the applied voltage, we show that you can modulate the magnitude of the cAMP gradient, and by turning the field on for the other electrode array in the symmetric device, we can switch the direction of the chemical gradient. We aim to demonstrate the usefulness of this device to study cellular migration under arbitrary chemical concentration gradients and steepness.

Advisor: Dr. Zachary Gagnon
Reader: Dr. Joelle Frechette

Acknowledgements

Here, I would like to take the opportunity to acknowledge all the people who helped me in these days. First and foremost, I would like to sincerely thank Dr. Zachary Gagnon for the opportunity to work in his lab on leveraging electrokinetic and microfluidic research since November 2016. Dr. Gagnon has selflessly shared his creativity and expertise with me. His contributions and guidance has helped improve the quality of my research.

Credits also go to my mentor, Nicholas Mavrogiannis, who has provided extensive guidance throughout my research and academic life at Johns Hopkins University. Dr. Mavrogiannis gladly took me under his wing when I first joined the Gagnon Lab and has helped me develop into the researcher I am today. Without his support, my thesis work would not be the same. Furthermore, I would like to thank all the members of the Gagnon Lab for creating a positive and enjoyable working environment. The members of the Gagnon lab have always been supportive of my research endeavors and, as a result, have made it a memorable experience overall.

In addition to the support of my lab, my peers have invaluably helped me achieve accomplishments in research, as well as in academic life. I would like to thank all my friends and colleagues that unfailingly fight alongside me to help me get to where I am today. Solving problems and overcoming obstacles with them have become unforgettable memories. Working with my friends and colleagues has shaped my personality and given me the strength to persevere in the face of major hardships–it has been a joy to work with them.

Last but not least, I would like to thank my parents, Morris and Nooshin Lavi, who made everything possible and have always supported me, emotionally and financially. My parents have fostered my tenacious work ethic and have help me develop into the man I am today. They are the best part of my life and continue to be the reason I strive to make my dreams into accomplishments. I would like to dedicate my thesis to my parents, whom I love deeply.

Table of Contents

List of Figures

List of Symbols

$\cdot$	Dot Operator
∇	Del Operator
∂	Partial Derivative Operator
Re[…]	Real Part of ...
β	Difference in Ion Number Densities
ε_o	Vacuum Permittivity
ε_r	Relative Permittivity
ε	Dielectric Constant
ε_i^*	Complex Permittivity
κ^{-1}	Debye Length
μ_i	Ion Mobility Coefficient of Species i
μ_o	Vacuum Permeability
μ_r	Relative Permeability
ρ_E	Charge Density
σ	Charge Electrical Conductivity
σ_f	Conductive or Free Surface Charge
σ_t	Total Surface Charge
σ_p	Bound or Polarized Surface Charge
τ_q	Charge Relaxation Time
Φ_i	Electric Potential of Species i
χ	Electric Susceptibility of the Dielectric
ω	Frequency
a	Diffusion Model Coefficient
C_i	Molar Concentration of Species i
D_i	Diffusion Coefficient of Species i
E_o	Magnitude of the Applied Electric Field
F	Faraday Constant
J_i	Ohmic Current of Species i
K	Polarizability Factor
L	Half the Width of the Electrode Separation
n_+	Positive Ion Number Density
n_-	Negative Ion Number Density
n_O	Unperturbed Ion Number Density
P	Polarization Vector
Re_{el}	Electrical Reynolds Number
t	Time
U_{EV}	Electroviscous Velocity Scale
X_{RMS}	Root Mean Squared Displacement
z_i	Valence Number of Species i

Chapter 1

Introduction

Electrokinetics is a field of study involving the interactions between charged interfaces and surfaces with an electric field. One particular electrokinetic phenomena, known as dielectrophoresis (DEP), involves the interaction between a non-uniform electric field and a polarizable particle, such as a red blood cell. In DEP, the electric field polarizes the particle surface and induces a charge dipole. This dipole then yields a dielectrophoretic particle force[1] that is responsible for producing particle motion (Figure 1 A and B). Negative dielectrophoresis causes motion of the polarizable particle to areas of low field strength, such as the center of the quadrupole electrode array, whereas, positive dielectrophoresis causes motion of the polarizable particle to areas of high field, such as the edges of the metal electrodes.

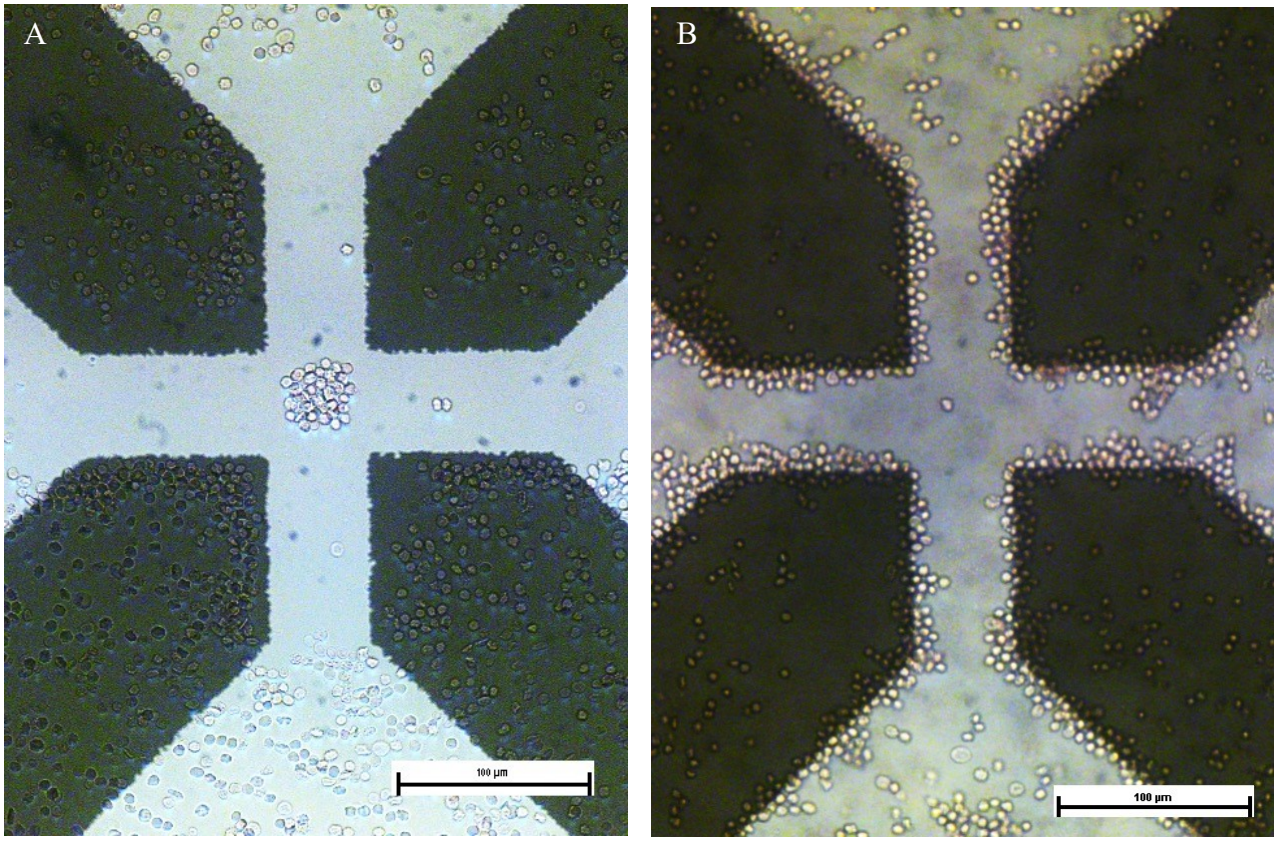

Figure 1. (A) Negative and (B) positive dielectrophoresis of red blood cells (RBCs) in a non-uniform AC field (100 µm scale bars).

Many electrokinetic processes depend on this interfacial phenomenon where the field drives ions or molecular dipoles to become non-uniformly polarized at interfaces of electrical mismatch (e.g. differences in electrical conductivity of dielectric constant). Recently, the physics responsible for DEP has been leveraged to manipulate liquid interface in what is now known as fluidic dielectrophoresis (fDEP).

With advancements in semiconductor fabrication, lab-on-chip (LoC) technology continues to be a promising avenue for use in many fields of science, including medicine and biology. A developing technology for point of care testing are microfluidic devices that exploit electrokinetic forces. LoC technologies offer many advantages to conventional diagnostics such as small fluid volumes, faster response time, high-throughput, portability and low-cost. The ability to control spatial and temporal concentrations gradients can be used to create *in vivo* mimicking LoC[2].

By integrating electrokinetic phenomena into fluidic systems, we hope to miniaturize high-end bio-analytical systems in medical and laboratory settings onto portable microchips. These miniaturized devices are limited by a slow rate of diffusive transport at the microscale, yet, immunoassays, such as DNA hybridization and cell-molecular interactions require rapid control of the chemical environment.

The objective of this work is to develop a new class of electrokinetic fluid switch for on-chip liquid routing and handling. We accomplish this using fDEP, where an electrical liquid-liquid interface is precisely controlled upstream. This fDEP-regulated flow is then driven into a downstream microfluidic environment where it is utilized for controlling the concentration and steepness of chemical gradients.

In particular, the goal of this project is to use fDEP to control and study cell motility in cells undergoing biased migration during chemotaxis. Many cellular organisms respond to specific chemical gradients through chemotaxis. Chemotaxis can be considered in various parts—directional sensing, potential sensing, modes of motility, and morphology. The rapid growth of the microfluidics field has led to new designs for gradient generators to investigate cellular motility[3]. A myriad of cell types have been studied for their ability to sense and respond to chemical gradients. For example, *Escherichia coli (E. coli)*, a common bacterium serving as a prokaryotic model organism, has a frequency dependent response to chemical gradients of *L*-aspartate[4]. This phenomenon is also apparent for neutrophils, a type of white

blood cell common to most mammals, that senses and migrates towards chemical gradients of various chemoattractants, such as the bacterial isolate tripeptide *N*-formyl-Met-Leu-Phe (fMLF)[5] and other chemokines.

Controlling the chemical microenvironment is a prerequisite for studying how physiological and pathological processes respond to chemical gradients[6]. Biological systems use signal transduction pathways to process chemical stimulus to intracellular signals to produce the appropriate cellular response. Further, enhanced fluidic control will enable a more robust study of the underlying mechanisms for cellular motility and the ability to easily screen and quantify the effects of potential chemokines.

In this work, we investigate the interactions between an external AC electric field and a microfluidic-generated liquid-liquid interface to develop the ability to controllably route fluid flows within the confines of a microchannel. We determine the effect of the AC electric field when applied perpendicularly to the surface of the liquid-liquid interface created by two miscible cell buffers. We then integrate this fDEP phenomena into a microfluidic gradient generator to create a platform for studying cell migration in response to our fDEP-regulated chemical gradients. This generator is then used to control the concentration of the chemoattractant, cyclic adenosine monophosphate (cAMP).

Chapter 2

Materials and Methods

2.1 Microelectromechanical Device Fabrication

Our microelectromechanical system (MEMS) (Figure 2 D) was fabricated using metal deposition, standard microfabrication, lithography and chemical etching techniques. The MEMS is comprised of a metal electrode and a polydimethylsiloxane (PDMS), an elastomeric material, microchannel layer that were fabricated from negative (Figure 2B and 2C) and positive (Figure 2A) polarity mylar photomasks, respectively, and bonded together in class-100 cleanroom. The designed photomasks were printed by FineLineImaging (Colorado Springs, Colorado) with a resolution of 50K DPI (dots per inch), which corresponds to a minimum feature size of 7µm.

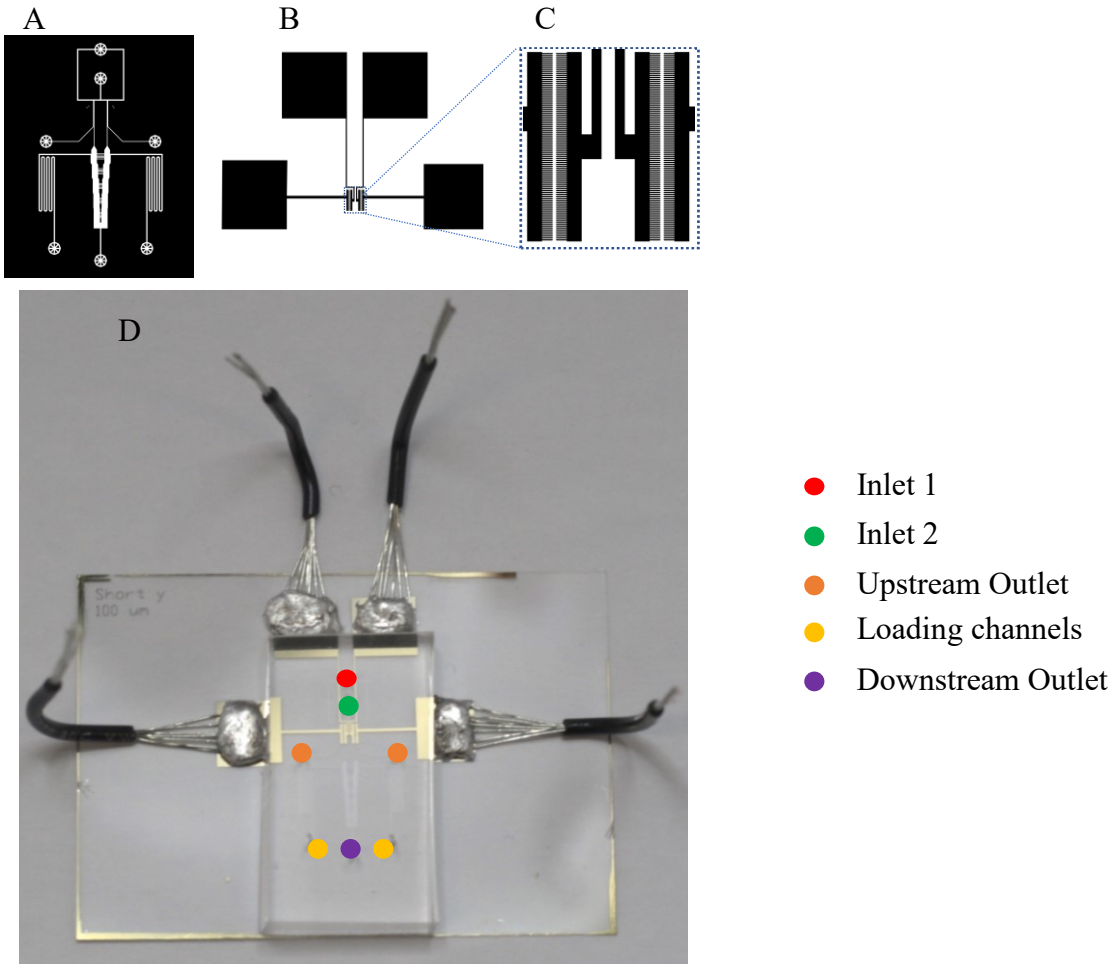

Figure 2. (A) Mylar photomask for flow layer (positive polarity). (B) Mylar photomask for metal electrode layer (negative polarity). (C) Blow up of electrode. (D) Image of a typical device.

2.1.1 Metal Deposition & Electrode Fabrication

The thin-film electrode layer was fabricated using vapor deposition and wet chemical etching techniques. Glass coverslips (50 x 30mm, no.1, Fisher Scientific) were coated with 20nm of chrome and 30nm of gold using electron beam evaporation. Electron beam evaporation is a common technique to uniformly deposit metal onto a surface. To coat the coverslips with metal, they are attached to a substrate holder that is placed at the top of the vacuum chamber. The gold-filled and chrome-filled crucibles are placed in the bottom of the vacuum chamber in a rotor to switch materials between deposition steps. Unlike gold, chrome directly adheres to glass and was used as an adhesion layer for the gold layer. By exposing the crucible to a 6.5 kV electron beam, the high current causes local heating and evaporation of the metal. The evaporated metal precipitates into the solid form and deposits onto all exposed surfaces within the chamber. To conclude the metal deposition, another metal, gold, was deposited onto the chrome-coated coverslip.

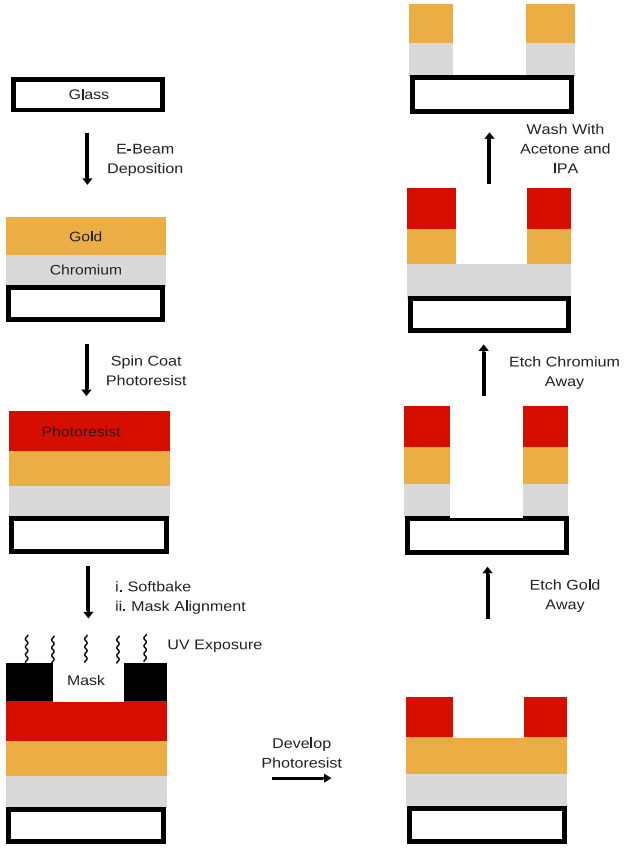

Figure 3. Schematic of a typical metal deposition and electrode fabrication procedure.

The chrome and gold covered coverslips were patterned by spin-coating a positive photoresist (Shipley 1318) at 3000 rpm with an acceleration of 200 rmp s^{-1} for 30 seconds. Then, the photoresist coated wafer was baked for two minutes at 95 ^{o}C followed by constant UV exposure of 85 mJ cm^{-2}. Since a positive photoresist was used, exposed photoresist crosslinked to the slide and unexposed photoresist was washed away by development in MF-26 for 2 minutes. To conclude the electrode patterning, the unexposed metal film was etched away with gold and chrome chemical etchant, creating the desired patterned metal electrodes. Lastly, the patterned slide was washed with acetone and isopropanol to remove any remaining photoresist.

2.1.2 Silica Master Mold & PDMS Fabrication

Rapid prototyping of microfluidics was accomplished by employing polymer molding and casting techniques that were originally adapted from the semi-conductor industry [7]. The process involves crosslinking a polymer onto a substrate and pouring or casting an elastomer material atop the polymer cross-linked substrate. Microchannels of Polydimethylsiloxane (PDMS), a commonly used material for microfluidic assays, were fabricated using SU-8 polymer molding techniques. A master mold was fabricated on a silica wafer using negative photoresist (SU-8 3050, Microchem Corp). The photoresist was spin-coated on the silica wafer to a height thickness of 50 μm (Dekta IIA). The photoresist-coated wafer was soft-baked at 65 ºC for 1 minute and pre-exposure baked at 95 ºC for 5 minutes. Next, a positive polarity mylar photomask was aligned with the wafer and UV exposed to produce strong acid that initiates SU-8 crosslinking of exposed areas. To conclude the crosslinking, the wafer was post-exposure baked at 95 ºC and developed in SU-8 developer. Lastly, the developed wafer was hard-baked at 200 ºC overnight to sharpen edges.

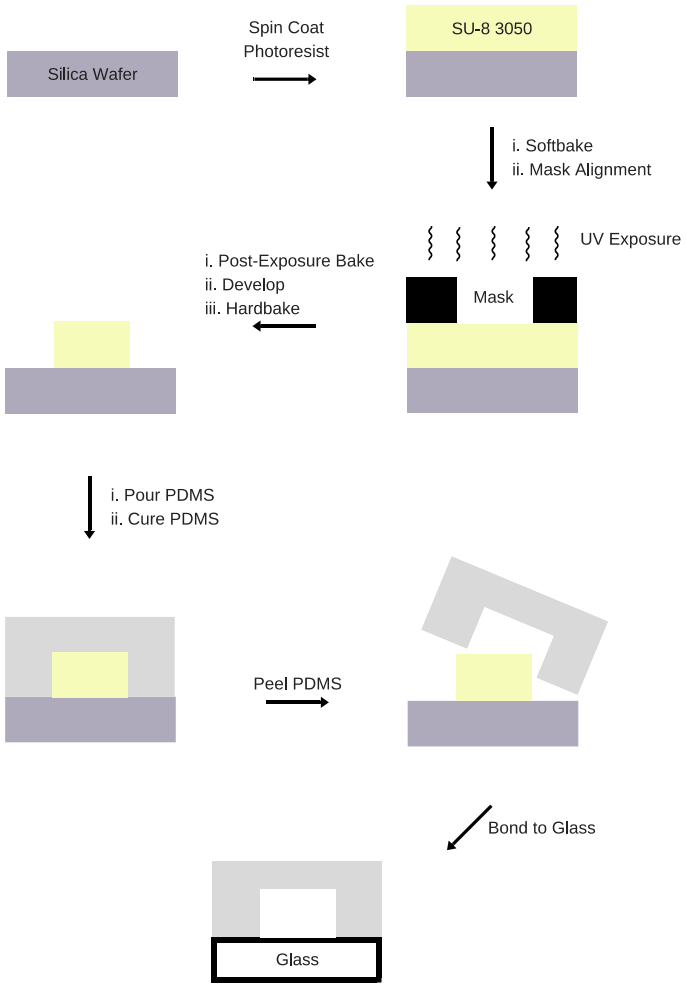

Figure 4. A schematic of the production of the silica master mold and PDMS flow layer.

The microchannel layer was fabricated in PDMS (Momentive, RTV 615A), a transparent elastomeric material commonly used for molding of microfluidic devices[8]. A 1:10 mixture of PDMS elastomer and curing agent was poured atop the lithographically fabricated SU-8 polymer mold, cured at room temperature and gently peeled off. The fluid ports were punched into the PDMS using a 0.75 mm biopsy punch (Ted Pella, Inc.).

2.1.3 Bonding

The microchannel and metal patterned coverslip were exposed to oxygen plasma (Jelight, Model 42A) for 1 minute and immediately aligned and sealed under an inverted microscope. Plasma was used to promote PDMS adhesion to the metal patterned coverslip by increasing silanol groups on the PDMS surface, which forms covalent bonds with coverslip and is responsible for the irreversible seal[8]. To finish bonding the chip, the bonded device was baked overnight at 85 ^{0}C. To connect the chip to a power supply, 1.50" of hook up wire was stripped by .25" on each end and soldered to each of the four electrode pads with indium**.**

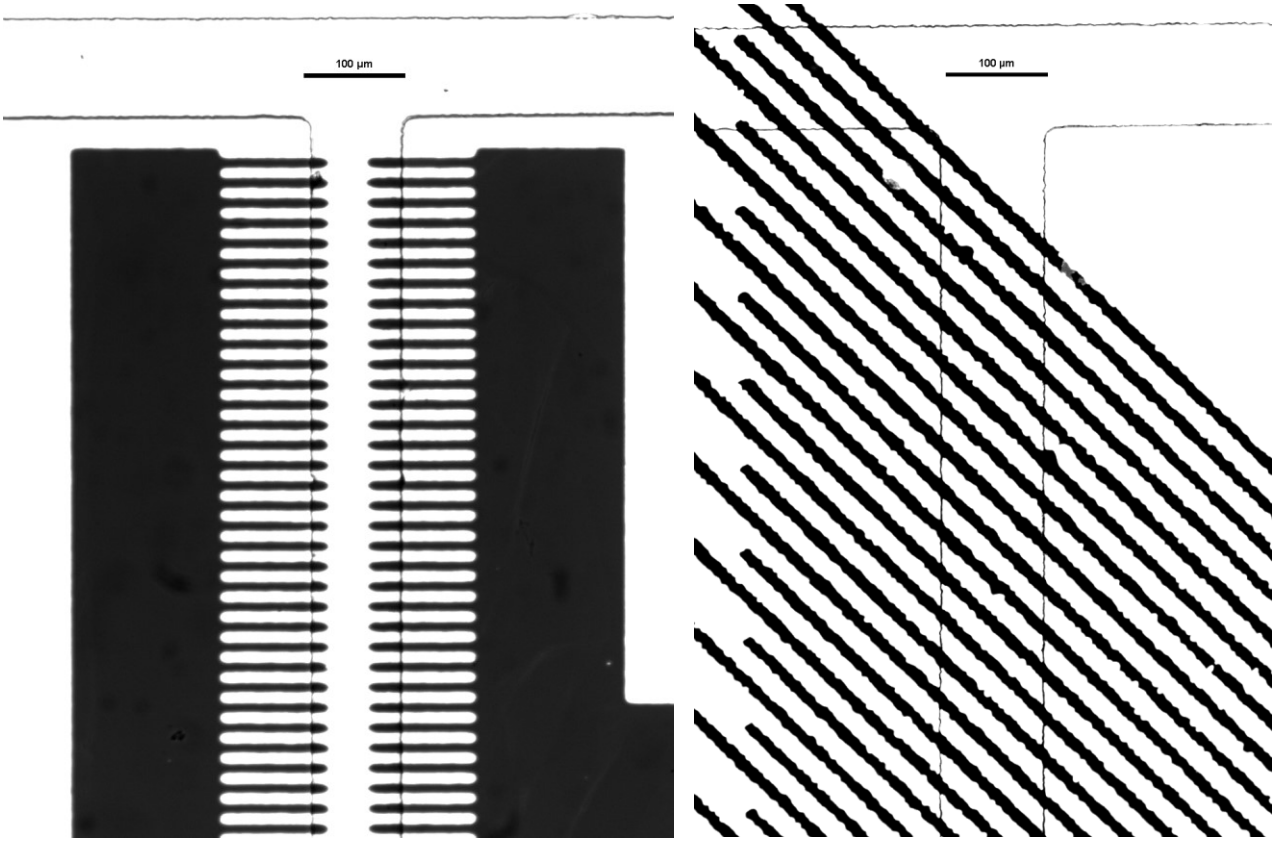

Figure 5. This two-panel figure depicts the 'teeth' (image on the left) and 'interdigitated' (image on the right) metal electrode arrays embedded with a 'T-channel'. Both brightfield images are 8bit monochrome images acquired with a Nikon microscope. The 'teeth' and 'interdigitated' electrode arrays have a separation of 40 and 15µm, respectively.

2.2 Chemical Solutions

The MEMS discussed in this paper have two inlet ports. Two fluids are driven through each inlet port by an Elveflow® Microfluidics Flow Control System. We characterized the amount that one fluid was deflected downstream by acquiring confocal micrographs at the

microfluidic junction at the end of the electrode array. For the control solutions, 6-aminohexanoic acid and phosphate buffered saline, we used fluids with mismatched conductivity and dielectric constant. For the buffered solutions, we used two variations of developmental buffer that had equal dielectric constant but disparaging electrical conductivities. For the control solutions, the green and red fluid streams are PBS and AHA, respectively. Whereas, for the buffer solutions, the green and purple fluid streams are the low conductive DB fluid and high conductive DB fluid, respectively.

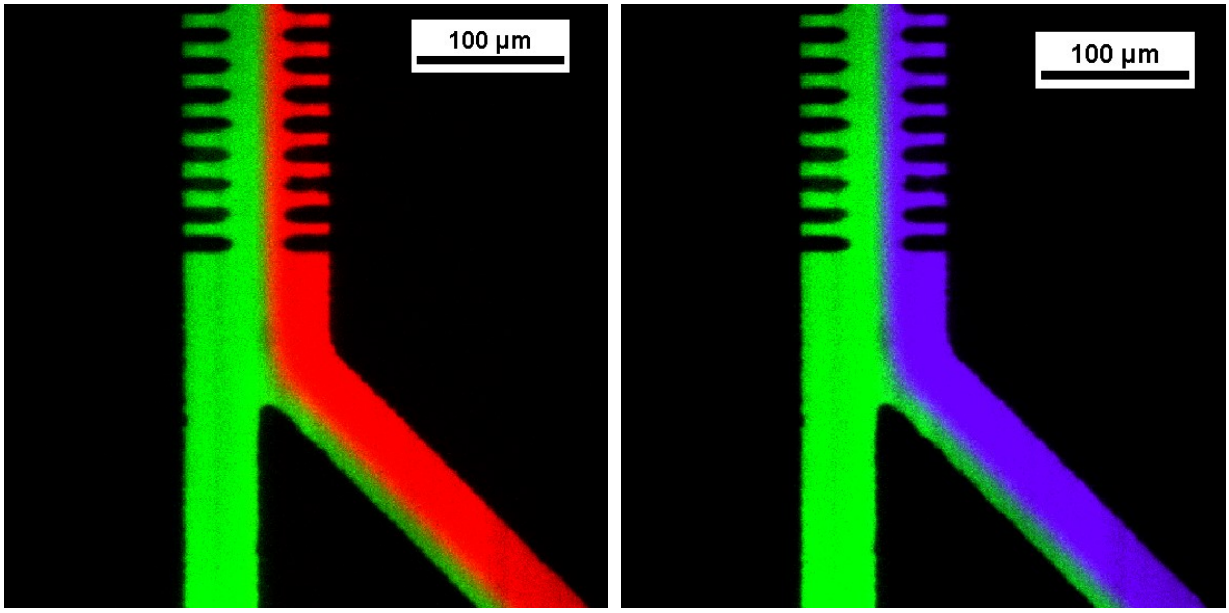

Figure 6. Confocal Images of the surface of the MEMS. (A) Control solutions: AHA + red fluorescent dye and PBS and green fluorescent dye. (B) Buffer solutions: high conductivity developmental buffer and purple fluorescent dye and low conductivity developmental buffer + green fluorescent dye.

2.2.1 Phosphate Buffer Saline and 6-Aminsohexanoic Acid

For the control solutions, the two fluids used were phosphate buffered saline (PBS) and 2M 6-aminohexanoic acid (Sigma Aldrich) (AHA). Fluorescent dyes were used as convective tracers to visualize the induced electrophoretic force. Solutions of 10 ng mL^{-1} of Alexa Fluor 488 (Invitrogen) a green and Alexa Flour 594 (Invitrogen) a red dye, were used for PBS and AHA, respectively. PBS, a common cell buffer used to maintain osmolality of cells in solution, was used as a high conductive fluid. AHA, a zwitterion commonly used to increase the dielectric constant of an aqueous solution, was used as the high dielectric fluid. Before labeling, AHA was vigorously shaken in 5g/mL Dowex MR-3 (Sigma Aldrich) ion exchange resin to remove salt

impurities and reduce solution conductivity. Since the fluorescent dyes are ionic, fluid conductivities were measured using a handheld conductivity meter after the addition of the tracers. Figure 8 depicts the interface of the two fluid streams, where green is the high conductivity PBS stream and the red is the high dielectric AHA. The PBS, or the high conductivity stream, had a conductivity of 58mS cm^{-1} and a dielectric constant $\varepsilon = 80$, whereas the high dielectric fluid had a conductivity of 17μS cm^{-1} and a dielectric constant $\varepsilon = 110$[8].

2.2.2 Developmental Buffer (DB)

To apply this technology to the study of cellular migration, we produced buffers that are biologically compatible with *Dictyostelium discoideum.* Namely, we utilized developmental buffer (DB) and adjusted the concentration of magnesium chloride and calcium chloride and produced variations of DB with disparaging conductivities and equal dielectric constant. All chemical compounds used for the DB stock solutions (Potassium Phosphate Monobasic (KH_2PO_4), Sodium Phosphate Dibasic Heptahydrate (Na_2HPO_4), calcium chloride ($CaCl_2$), Magnesium Chloride Hexahydrate ($MgCl_2 \cdot 6H_2O$) and cAMP) were purchased from Sigma Aldrich.

Prior to use, the stock solutions were made and autoclaved at 250 ^oF for 50 minutes. The two working solutions, (1) developmental buffer (DB, 5mM KH_2PO_4, 5 mM Na_2HPO_4, 1mM $CaCl_2$ and 2mM $CaCl_2$) and (2) developmental buffer with low calcium concentration (DB low Ca^{2+}, 5mM KH_2PO_4, 5 mM Na_2HPO_4, 1mM $CaCl_2$, 2mM $CaCl_2$ and 200 nM cAMP), were made from the stock solutions and the pH of each solution was adjusted to a physiological pH of 6.4 with hydrochloric acid (HCl). Solutions of 10 ng/mL of Alexa Fluor 647 (Invitrogen) and Alexa Flour 488 (Invitrogen) were used for the high and low conductivity DB, respectively. At a physiological pH of 6.4, both fluids had a dielectric constant of approximately 80, whereas, the standard DB and the low $CaCl_2$ and $MgCl_2$ DB had conductivities of 1.87 and 1.67mS cm^{-1}, respectively.

2.2.3 cAMP as a Secondary Messenger for Dictyostelium discoideum

Signal transduction through G-protein-coupled receptors (GPCR) are central to practically all cellular functions. These membrane-bound receptors register sensory messages from their chemical environment and produce specific cellular functions. These signals can activate the G-protein causing the release of secondary messengers (cAMP, IP_3, Ca^{2+} etc.) and

resulting in a myriad of cellular responses[9]. *Dictyostelium discoideum* () is a social amoeba and a model organism to study the cAMP activation of GPCR and its role in regulating chemotaxis.

cAMP has molecular interactions with virtually all living organisms and plays a key role in signal transduction pathways through surface receptors. Uptake of cAMP can result in structural changes that affect the dominate mode of motility for *D. discoideum* cells. These cells have been shown to migrate towards chemical gradients of cAMP by extending their leading edge by two types of protrusion: (1) pseudopods that are driven by actin polymerization and (2) membrane blebs that are driven by osmotic pressure[10].

2.3 Flow System

Samples were delivered to the microfluidics device using an ELVEFLOW microfluidic flow controller depicted in figure 7. House gas is used as a pressure supply to the flow controller that pressurizes the inlet sample reservoirs and drives fluid through the device[11]. The low Reynolds number associated with microfluidic flow results in a laminar flow profile and slow diffusive timescale. As seen in Figure 8, these attributes allow two fluids of varying electrical properties to flow side-by-side in a microfluidic channel without diffusively mixing.

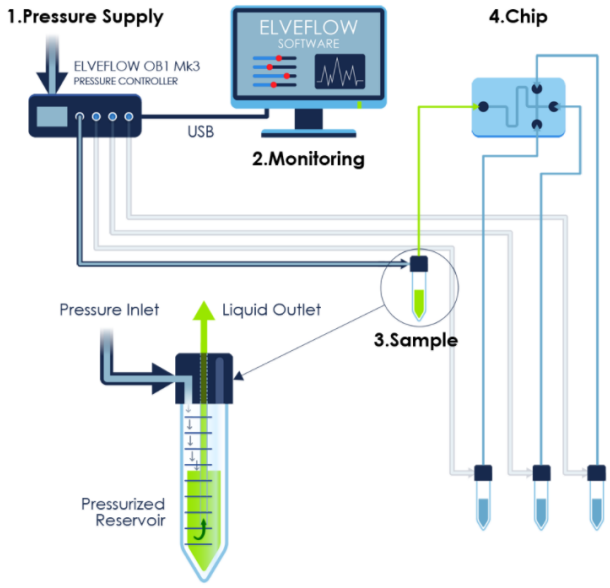

Figure 7. Schematic of the ELVEFLOW flow control[11].

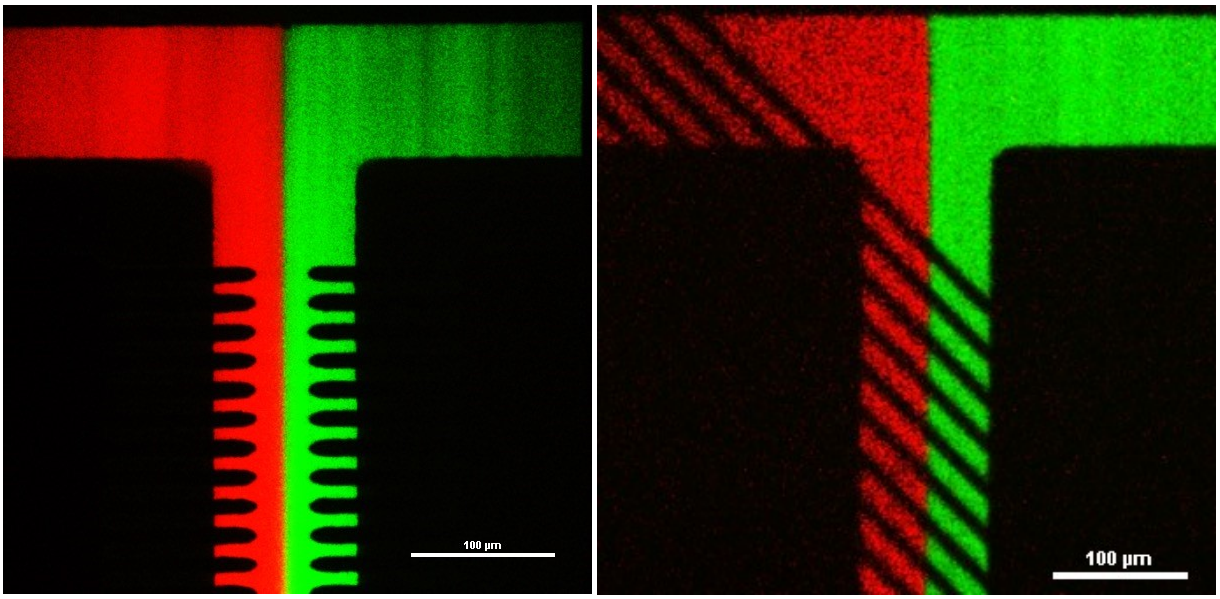

Figure 8. Confocal images of the surface of the MEMS devices. (A) The image on the left is for the MEMS with embedded teeth electrodes (B) is for the embedded interdigitated electrodes.

2.4 Function Generator

Deflection at the interface is achieved by applying varying frequencies and voltages across the liquid-liquid interface of the microfluidic device. The resulting fluid displacement at the interface flows past a y-junction allowing the deflected fluid to flow downstream. To characterize the span of concentrations we could achieve, we applied 5, 10, 15, and 20 Volts peak-to-peak (V_{pp}) at four frequencies of 5, 10, 15, and 20MHz using Function generator (Rigol DG 4162). We chose to operate our low frequency conditions at 5MHz due to future plans of utilizing an amplifier that typically cannot amplify frequencies below 5MHz.

Figure 9. Rigol DG 4102 Function Generator used to deliver an AC electric field with varying frequencies and voltages across the liquid-liquid interface of the microfluidic device[12].

2.5 MATLAB Method for Cross-section Analysis

To clearly observe and analyze the electrokinetic effects on the liquid-liquid interface, 3D confocal micrographs were acquired with a Nikon Eclipse Ti swept field confocal microscope. The microscope was equipped with an Andor iXon 897 camera, four 50 mW solid-state lasers for excitation and a 60x oil-objective. As seen in figure 10, acquired images were analyzed by a custom MATLAB method to first identify the interface in a coordinate system and fit a polynomial to this interface to determine the fraction of the cross section that was predominately one color. Next, since mixing of the co-flowing solutions are limited by the slow rate of diffusion, we determined the fraction of pixels with greater intensity of either color to determine the percentage of red and green in the cross-section. This information was used to determine the amount of deflection under varying voltages and frequencies.

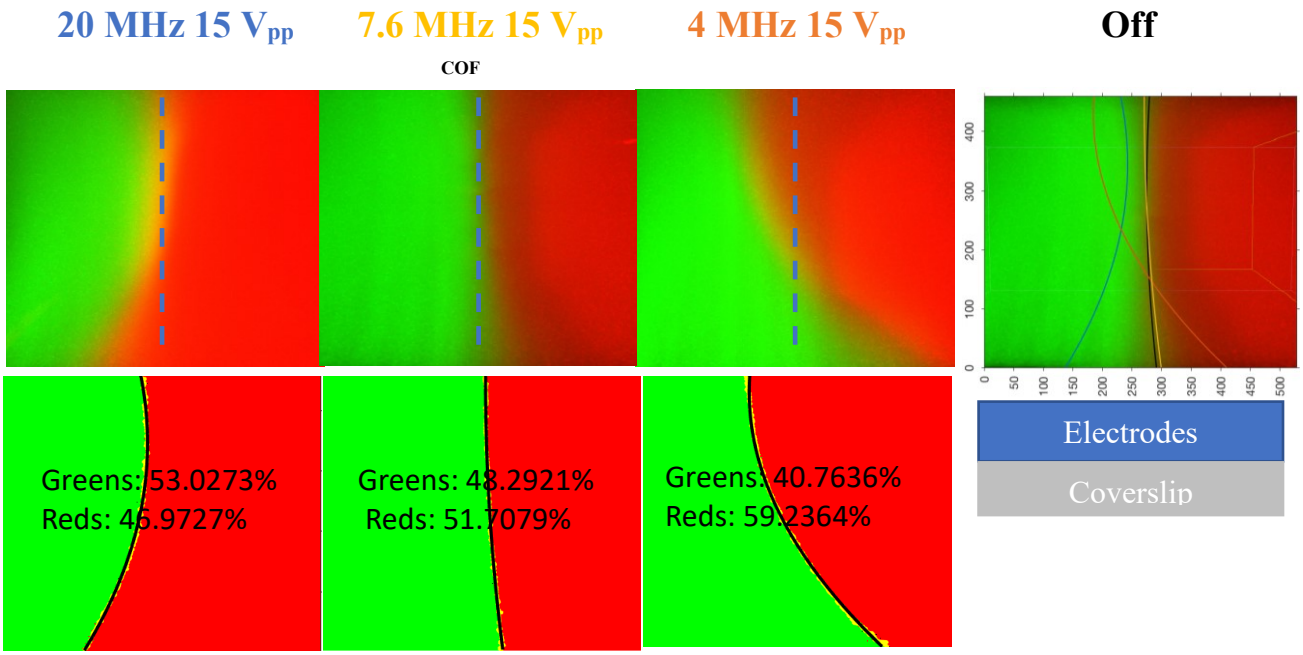

Figure 10. Panel of images demonstrating the input (the top row of images) to our custom MATLAB method, as well as, the output (the bottom row of images). We use this method to determine the fraction of the cross-section that was predominately one color. Additionally, we identify the interface (the rugged yellow curve in the bottom row of images) and fit a polynomial to the interface position (black line in the bottom row of images). We also overlaid the interface positions on a cross-section image where the field was off (blue curve is for an applied electric field of 20 MHz 15 V_{pp}, the yellow curve is for the cross-over frequency 7.6 MHz and 15 V_{pp} the orange curve is for 4 MHz 15 V_{pp}, and lastly the black curve is for the interface when no electric field is applied.

Chapter 3

Theoretical Background

The motion of particles and fluids have been a major focus for biological and chemical analysis. Conventionally, diffusion suggests the spreading of particles due to their Brownian motion. The particle displacement in time, *t,* is expressed by the root mean squared displacement and depends on the diffusion coefficient of the particle in solution, *D*, which is represented as

$$X_{RMS} = \sqrt{aDt} \qquad \textbf{[Equation 1]}$$

where a is the factor for the diffusion model and is 2, 4, or 6 for the 1D, 2D, and 3D displacement model, respectively. By incorporating microelectrode fabrication and lab-on-a-chip technology, there is great potential for exploring and exploiting AC or DC electric fields with particles and fluids interfaces. Unlike diffusion, this deflection is due to an active force. In this chapter, we describe underlying principles and theory of AC electrokinetics focusing on its applications for precise on chip fluid-routing.

3.1 Electrical Forces

Electrical forces such as electrophoresis (EP) and dielectrophoreis (DEP) act on both particles and fluids producing body forces and a net hydrodynamic stress that results in fluid motion. EP is the result of an electric field interacting with a fixed net charge, whereas DEP occurs in the presence of induced charges or polarizable materials. Electric fields produce a force per unit area on fluids or particles that have variations or gradients in charge density. Charges are mobile in an AC electric field, but the time averaged force in a single cycle is zero, as the charges move in opposite directions for each half cycle. Yet, in a non-uniform electric field, this force produces a constant fluid motion due to variations in conductivity and permittivity of the materials. Conductivity is a measure of how easily charge moves through materials and permittivity is a measure of how easily a material can orient in the presence of an applied electric field. Both the conductivity and the permittivity of the materials are important parameters for modeling the interfacial fDEP[8].

3.1.1 The Helmholtz Model

In the 1850's, Hermann von Helmholtz introduced a model for charged species and oriented dipoles at electrode-solution interfaces—the *electrical double-laye*r (EDL). This theory describes that the ionic environment near a charged surface is not as evenly distributed but is concentrated at the charged surface. This model assumes (1) no electron transfer reactions occur at the electrodes and (2) a purely electrolyte solution. The interactions between the ions in solutions and the charged surface were assumed to be electrostatic and resulted from the electrode that holds charge density from excess of electrons at the surface. Therefore, to maintain net charge neutrality, the charge held on the charged surface must be balanced by the re-distribution of ions close to the surface. Helmoltz's EDL can be formulated as a parallel plate capacitor with a linear relationship between stored charge and voltage drop. A limitation of this model is that it treats the differential capacitance as a constant, which is not indicative of physical systems[13].

3.1.2 Gouy and Chapman Contributions

There have been several modifications to the EDL theory proposed by Helmholtz. Namely, Gouy (1910) and Chapman (1913) independently proposed the idea of the *diffusive double layer*. The theory proposes that counter-ions are not rigidly held, rather, they diffuse into the liquid until the counter potential established by their departure restricts this movement. By analytically solving the Poisson-Boltzman (PB) equation, they describe the electric potential with respect to the distance from the electrodes, as well as the ion concentrations. The theory proposed by Gouy and Chapman assumes an ideal solution of point charges and that the activities are equal to the molar concentration. This is an appropriate approximation for ions far from the charged surface but not for the ion concentration close to the charged surface[13].

3.1.3 Stern Contributions

Although modifications to the electrical double layer proposed by Gouy and Chapman provide a better approximation, it still has limitations. Stern (1947) addresses the limitation of assuming point charges by incorporating the finite size of charges in his model. His improved model accounts for the adsorption of ions to the surface, as well as the limitation of how close the ions can to the surface due to their finite size. The stern and bulk regime meet at what is

known as the slipping plane, which corresponds to the distance that the potential decreases to the zeta potential[13].

3.1.3 Grahame Contributions

Shortly after, Grahame (1947) used the Gouy and Chapman model to relate the potential at the surface to the surface charge density. By employing Gauss' Law and the concept of charge neutrality, Grahame relates the charge in the diffusive layer to the negative of the surface charge. By solving the one dimensional PB equation and the condition that infinitely away from the charge surface the potential is approximately zero, Grahame determined an analytical expression for the charge distribution and the Debye length. Today, the Debye length is used as a measure of the net effect and magnitude of electrostatic interactions in solution[13].

3.2 Electrical Forces at Interfaces

As an electric field is applied across a liquid-liquid interface, charge polarizes and accumulates at the interface, which is dependent on both the field strength and the difference in electrical properties of the two materials or fluids. To maintain net charge neutrality, ions of opposite charges are attracted to the interface forming a layer of counter-ion charge, known as the double-layer. An applied electric field across a liquid-liquid electrical interface does not move the charges instantly, rather, it takes a few microseconds to reach equilibrium. The movement of free charges or the movement of charges at the interface is frequency-dependent, such that at low frequencies, free charges movement can keep up with the changing direction of the electric field, whereas at high frequencies the polarization of bound charges dominates.

3.2.1 Fluidic Dielectrophoreis by Maxwell-Wagner Polarization

Maxwell-Wagner (MW) is a classical electromagnetic theory that describes the movement and polarization of the interface of two co-flowing fluids and is driven by differences in charge relaxation times of the two materials. On a macroscopic level, the relaxation time of each material can be defined by the ratio of the materials dielectric constant and conductivity. When current flows in an insulated system across the interface, the difference in relaxation times enables charge accumulation at the interface. This MW effect can be employed to account for charge accumulation at most interfaces of two materials, but this study will focus specifically on the ability of MW polarization to deliver a controlled amount of chemoattractant and establish a chemical gradient for cells in confinement.

To understand the deflection within our microfluidic devices, we have established a theoretical formulation of fluidic dielectrophoreis at liquid-liquid electrical interfaces in previous work[6]. We begin by considering conservation equations for a dilute, two species electrolyte solution:

$$\frac{\partial C_1}{\partial t} + u \cdot \nabla C_1 = \mu_1 \nabla \cdot (z_1 \mathrm{F}\, C_1 \nabla \Phi) + D_1 \nabla^2 C_1 \quad \textbf{[Equation 2]}$$

$$\frac{\partial C_2}{\partial t} + u \cdot \nabla C_2 = \mu_2 \nabla \cdot (z_2 \mathrm{F}\, C_2 \nabla \Phi) + D_2 \nabla^2 C_2 \quad \textbf{[Equation 3]}$$

where C_i is the molar concentration, μ_i is the ion mobility coefficient, F is the Faraday constant, D_i are the diffusion coefficients and z_i are the valence numbers and Φ is the electric potential. To simply the formulation, we redefine the two species concentrations (C_1, C_2) in terms of charge electrical conductivity (σ) and charge density (ρ_E):

$$\rho_E = \sum_{i=1}^{2} F \mu_i C_i \quad \textbf{[Equation 4]}$$

$$\sigma = \sum_{i=1}^{2} \mu_i z_i^2 F^2 C_i \quad \textbf{[Equation 5]}$$

Assuming 1:1 symmetric electrolyte with $\mu = \mu_1 = \mu_2$, $D = D_1 = D_2$, and $z_1 = -z_2 = 1$, we rearrange the conservation equation by combining Equation 2 and 3 and substituting Equations 4 and 5 to arrive at,

$$\frac{\partial \rho_E}{\partial t} + u \cdot \nabla \rho_E = \nabla \cdot (\sigma \nabla \Phi) + D \nabla^2 \rho_E \quad \textbf{[Equation 6]}$$

The charge conservation is rendered non-dimensional by introducing the following characteristic scales:

$$[u] \sim U_{EV}, \quad [L] \sim L, \quad [t] \sim \varepsilon\sigma, \quad [\rho_E] \sim \frac{\varepsilon E_o}{L}, \quad [\Phi] \sim E_o L, \quad [\sigma] \sim \mu z F \rho_E \sim \mu z F E_o \varepsilon$$

U_{EV} is the electroviscous velocity scale, L is half the width of the electrode separation and E_o is the magnitude of the applied electric field. An important and measurable characteristic of the electrolyte is the time require for an ion to diffuse a distance on the order of a Debye length (κ^{-1}), which is known as the charge relaxation time (τ_q).

$$\kappa = \sqrt{\frac{D \varepsilon_o \varepsilon_r}{\sigma}} \quad \textbf{[Equation 7]}$$

$$\tau_q = \frac{\varepsilon_o \varepsilon_r}{\sigma} \quad \textbf{[Equation 8]}$$

The non-dimensional charge conservation becomes:

$$\frac{\partial \rho_E}{\partial x} + Re_{el} u \cdot \nabla \rho_E = \left(\frac{1}{\kappa \mathrm{L}}\right) \nabla \cdot (\sigma \nabla \Phi) + D \nabla^2 \rho_E \quad \textbf{[Equation 9]}$$

where, $Re_{el} = \frac{U_{EV}\varepsilon}{\sigma L} \sim 10^{-10}$ and is the Electrical Reynolds Number. Re_{el} resembles the ratio of the magnitude of convective to conductive current and demonstrated the dominating contribution is the conductive current. Furthermore, the electric Reynolds number is much less than unity and can be neglected. Lastly, the relaxation time (τ),

$$\tau = \frac{\varepsilon D}{\sigma \mathrm{L}^2} \sim 10^{-6} \qquad \textbf{[Equation 10]}$$

which is the ratio of charge relaxation to diffusive timescale. As the Debye length is on the order of several nanometers and is much smaller than the length scale of the system, the charge relaxation dominates over diffusion and is the primary transport term. Equation 10 reduces to,

$$\frac{\partial \rho_E}{\partial t} - \nabla \cdot (\sigma \nabla \Phi) = 0 \qquad \textbf{[Equation 11]}$$

Applying Gauss' Law ($\nabla \cdot (\varepsilon \mathrm{E}) = \rho_E$) on the micrometer length-scale suggests electrolytes are electroneutral and the difference in ion number densities are approximated by

$$\beta = \frac{n_+ - n_-}{n_+ + n_-} = \frac{\nabla \cdot (\varepsilon \mathrm{E})}{n_O} \qquad \textbf{[Equation 12]}$$

where n_O is the unperturbed ion number density and n_+ and n_i are the positive and negative ion number densities, respectively. The values for this system are $E_O \sim 10^5 \ \frac{V}{m}$, $\mathrm{L} \sim 100\mu\mathrm{m}$, and $\beta \sim 4X10^5$. In our system, the liquid is quasi-electroneutral and the one dimensional electric field is given by the solving the Laplace equation.

$$\nabla^2 \Phi = 0 \qquad \textbf{[Equation 13]}$$

3.2.2 Interfacial Surface Charge

The bulk electrolyte solution is considered quasi-electroneutral. However, at the interface, free and bound charges are induced and the charge conservation equation must be imposed on the system. First, we require the electric potential to be constant across the liquid-liquid interface,

$$\Phi_1 - \Phi_2 = 0 \qquad \textbf{[Equation 14]}$$

Charge accumulates at the interface due to non-uniform distribution free charge and perturbed bound charge at the interface. To satisfy the charge conservation equation, we apply Equation 8 and substitute the volume charge density (ρ_E) with the surface charge density (σ_f) since free and bound charge exist only at the interface. Then Equation 9 becomes,

$$\frac{\partial \sigma_f}{\partial t} = J_2 - J_1 \quad \textbf{[Equation 15]}$$

where J_1 and J_2 are the ohmic currents of fluid phase 1 and 2. The bound electric surface charge represents the electric displacement of free surface charge due to dielectric polarization. The displacement current is defined by

$$\varepsilon_1 E_1 - \varepsilon_2 E_2 = \sigma_f \quad \textbf{[Equation 16]}$$

In a harmonic field ($\frac{\partial}{\partial t} = j\omega$), equation 15 and 16 can be combined to arrive at the expression for charge conservation at the electrical liquid-liquid interface,

$$\left[\varepsilon_1 E_1 - \frac{j\sigma_1}{\omega}\right] E_1 = \left[\varepsilon_2 E_2 - \frac{j\sigma_2}{\omega}\right] E_2 \quad \textbf{[Equation 17]}$$

where the complex permittivity, ε_i^*, is given by $\varepsilon_i^* = \varepsilon_i - \frac{j\sigma_i}{\omega}$ is and the imaginary number, j, is given by j =$\sqrt{-1}$. From equation 17, we can see that at low frequency, as $\omega \longrightarrow 0$, interfacial prolarization is predominately driven by differences in electrical conductivity, whereas, at high frequencies, $\omega \longrightarrow \infty$, the polarization is driven by differences in electrical permittivity.

We derive a theoretical relation for the induced interfacial charge to the applied electric field and the electrical properties. First, it is helpful to note that the total surface charge, σ_t, at the electrical liquid-liquid interface is the sum of free or conductive surface charge (σ_f) and bound or polarized surface charge, σ_p, such that $\sigma_t = \sigma_f + \sigma_p$. By applying Gauss' law at the interface, we can obtain the free surface charge. The bound surface charge is give the divergence of the polarization vector, P, and is defined as:

$$\sigma_p = -\nabla \cdot \mathrm{P} = -(P_1 - P_2) \quad \textbf{[Equation 18]}$$

Dielectrics are materials that polarize in the presence of an electric field and are by in large linear and isotropic, with P linearly proportional to the electric field such that

$$\mathrm{P} = \varepsilon_o \chi E = \varepsilon_o(\varepsilon_r - 1)E \quad \textbf{[Equation 19]}$$

Where χ is the electric susceptibility of the dielectric. By combing Equation 16 and 18, the total induced interfacial charge becomes,

$$\sigma_t = \varepsilon_o(E_1 - E_2) \quad \textbf{[Equation 20]}$$

This expression is useful in understanding surface charge density at liquid-liquid electrical interfaces that undergo Maxwell-Wagner polarization mechanics.

3.2.3 One Dimensional Model

Our microfluidic system consists of two co-flowing liquid streams, each with a conductivity and dielectric constant. As discussed earlier, the two fluid streams do not convectively mix due to low Reynolds number of microfluidic flow. Upon entering the electrode array, z=0, the liquid-liquid interface is subjected to an external field that concludes at z=L_e, where there is a junction to split the fluid streams to either the outlet or the cell chambers. We begin by modeling the electric field distribution at the microchannel cross section and derive a frequency dependent surface charge density at the interface.

As the coplanar electrodes are embedded on the surface of the microchannel, y =0, and the electric field decays exponential, the greatest magnitude of interfacial electrical stress will occur on the surface of the microchannel. Although it is possible to analytically determine the electric field distribution in 2D, we will reserve this type of model for future work.

In this paper, we present a 1D model for the electric field distribution on the channel surface to determine the induced surface charge at the interface. By employing the exponential time dependence for the electric field ($e^{i\omega t}$), the instantaneous applied field at time *t* and location *x* on the channel surface is given by,

$$E(x,y) = Re[E(x,y=0)e^{i\omega t}] \qquad \textbf{[Equation 21]}$$

where Re[…] represents the real part of the complex electric field phasor. Now, we can solve the one-dimensional Laplace equation for each species $\left(\frac{\partial^2 \Phi_i}{\partial x^2} = 0\right)$. First we define the center of the microchannel to be the mid-plane and the location of the electrodes to be a distance of L and –L from the center. By specifying the potential at the electrodes $\Phi(\mathrm{L}) = \mathrm{V}_1$ and $\Phi(-\mathrm{L}) = \mathrm{V}_1$ and applying the boundary conditions given in Equation 14 and 17, the field solutions are:

$$\frac{\partial \Phi_1}{\partial x^2} = \frac{\varepsilon_2^*}{\varepsilon_2^* + \varepsilon_1^*} E_o \qquad \textbf{[Equation 22]}$$

$$\frac{\partial \Phi_1}{\partial x^2} = \frac{\varepsilon_1^*}{\varepsilon_2^* + \varepsilon_1^*} E_o \qquad \textbf{[Equation 23]}$$

where $\mathrm{E_o}$ is the magnitude of the applied electric field $\left(E_o = \frac{V_2 - V_1}{2L}\right)$. Therefore, using Equation 16 the total surface charge can be expressed as:

$$\sigma_t = \varepsilon_o \left(\frac{\partial \Phi_1}{\partial x} - \frac{\partial \Phi_2}{\partial x}\right) = \varepsilon_o \left(\frac{\varepsilon_2^* - \varepsilon_1^*}{\varepsilon_2^* + \varepsilon_1^*}\right) E_o \qquad \textbf{[Equation 24]}$$

Taking the time-average over the period of the monochromatic field ($t = \frac{2\pi}{\omega}$), the time-averaged surface charge density at the liquid-liquid interface is:

$$\sigma_t = Re\left[\frac{\varepsilon_2^* - \varepsilon_1^*}{\varepsilon_2^* + \varepsilon_1^*}\right]\left(\frac{\varepsilon_o E_o}{2}\right) \quad \textbf{[Equation 25]}$$

Thus, the time averaged force per unit area of fluidic dielectrophoresis (DEP) at the surface of the microchannel is:

$$F_{fDEP} = \sigma_t E = Re\left[\frac{\varepsilon_2^* - \varepsilon_1^*}{\varepsilon_2^* + \varepsilon_1^*}\right]\left(\frac{\varepsilon_o E_0^2}{2}\right) \quad \textbf{[Equation 26]}$$

Equation 20 illustrates that the induced surface charge and consequently the induce electric interfacial force is zero when

$$Re\left[\frac{\varepsilon_2^* - \varepsilon_1^*}{\varepsilon_2^* + \varepsilon_1^*}\right] = 0 \quad \textbf{[Equation 27]}$$

This frequency dependent expression includes a critical frequency at which the induced surface charge is zero, thereby producing no electrical force on the interface. In terms of DEP, this frequency is known as the cross-over frequency (ω_{cof}), and in terms of fDEP the cross-over frequency is:

$$\omega_{cof} = \frac{1}{2\pi}\left[\frac{(\sigma_1 - \sigma_2)((\sigma_1 + \sigma_2)}{(\varepsilon_2 - \varepsilon_1)(\varepsilon_2 + \varepsilon_1)}\right]^{1/2} \quad \textbf{[Equation 28]}$$

The interfacial surface charge at a particle-liquid interface produces an induced dipole moment across the particle. This moment interacts with an external non-uniform electric field and drives its motion in a suspended media. The magnitude and direction of the particle-liquid DEP force is frequency dependent and is called the Cluasius-Mossotti (CM) factor. The CM factor describes the frequency dependent polarizability of the interface. For a homogenous isotropic sphere the time-averaged DEP force is expressed as[1]:

$$K(\omega) = \frac{\varepsilon_p^* - \varepsilon_L^*}{\varepsilon_p^* + 2\varepsilon_L^*} \quad \textbf{[Equation 29]}$$

where $K(\omega)$ is the CM factor for a sphere, and ε_p^* and ε_L^* are the complex permittivity of the particle and the liquid, respectively. For fluidic dielectrophoresis, the polarizability factor is expressed as[7]:

$$K(\omega) = \frac{\varepsilon_2^* - \varepsilon_1^*}{\varepsilon_2^* + \varepsilon_1^*} \quad \textbf{[Equation 30]}$$

In our work, we observe a similar effect at the liquid-liquid interface, where the fluid motion is proportion to the real part of the part of the polarizability factor. This factor is a complex function of frequency, conductivity and permittivity expressed as:

$$Re[K(\omega)] = \frac{(\varepsilon_2-\varepsilon_1)\tau^2\omega^2}{(\varepsilon_2+\varepsilon_1)(\tau^2\omega^2+1)} + \frac{(\sigma_2-\sigma_1)\tau^2\omega^2}{(\sigma_2+\sigma_1)(\tau^2\omega^2+1)} \quad \textbf{[Equation 31]}$$

where $\tau = \frac{(\varepsilon_2+\varepsilon_1)}{(\sigma_2+\sigma_1)}$ is the characteristic Maxwell-Wagner charge relaxation timescale at the interface between the two liquids.

In particle-liquid DEP, the induced dipole moment is symmetric and a non-uniform field is required to produce a nonzero DEP force. However, in fDEP, polarization of the interface does not require a dipole moment, and consequently, it does not require a non-uniform electric field to produce a nonzero DEP force.

Chapter 4

Results and Discussion

Microfluidic devices have gained interest for their ability to mimic microvasculature systems. However, these devices are limited by their inability to actively route fluids. The force that is produced by applying an electric field across a metal electrode in contact with liquid-liquid interface results in a fluid motion that can be explained by MW polarization mechanics. Conventionally, this motion is discussed the context of particle-liquid interfaces and is dubbed dielectrophoresis, whereas, in terms of liquid-liquid interfaces it is called fluidic dielectrophoresis. In this paper, we present a method to exploit the dependence of the polarizability factor by controlling intrinsic fluid properties—electrical conductivity and permittivity.

By employing fluidic dielectrophoresis, we analyzed on-chip fluidic dielectrophoresis of a liquid-liquid interface as an application to mimic cellular microenvironments for chemical signaling and chemotaxis research on a single-cell level. As seen in Figure 11, we have demonstrated the ability to control chemical microenvironment in downstream connecting microchannels using our active solid-state electrokinetic switch.

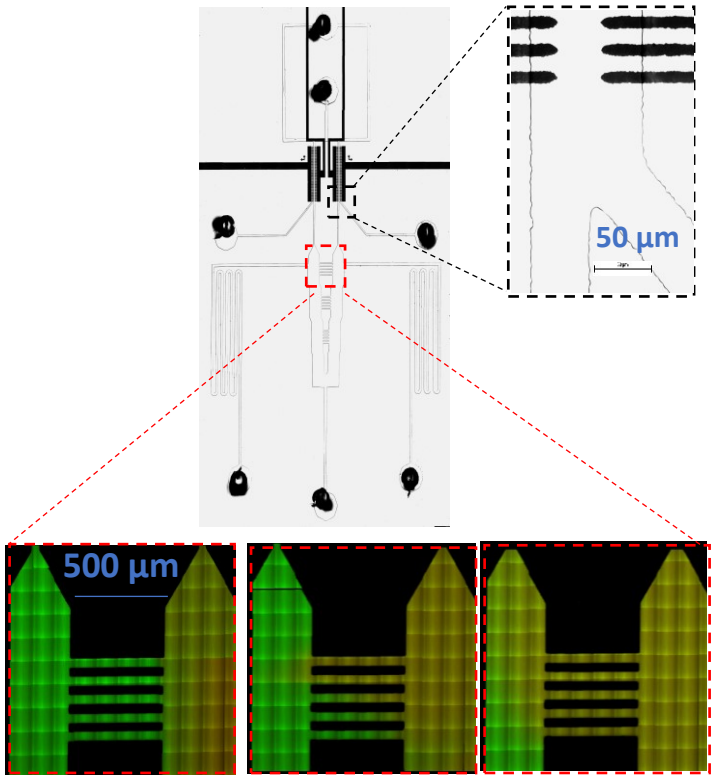

Figure 11. An image illustrating the ability to establish a chemical gradient in connecting microchannels using a solid-state switch. The confocal images are taken of the PBS/AHA fluid system using an applied electric field of 20 MHz and 20 V_{pp} and images were taking every 15 minutes for 45 minutes.

4.1 Induced Surface Charges in Fluidic Dielectrophoresis

Unlike conventional DEP, where particle motion results from the interaction of a non-uniform electric field with an induce particle dipole moment, fDEP fluid motion results from the electric field interacting with induced surface charges at the liquid-liquid interface. The real part of the polarizability factor is a function of frequency and can be employed to determine the COF and both the high and low frequency asymptotes terms. At low frequencies, or frequencies below the COF, the high conductive fluid will conduct charge faster than can be removed by the low conductive fluid. Therefore, at the low frequency regime, interfacial polarization is dependent solely on the electrical conductivity of each fluid. At high frequencies, or frequencies above the charge relaxation timescale, the electric field oscillates faster than charges can migrate to the interface. Thus, conductive charge does not have sufficient time to occur in each half-cycle and interfacial polarization is driven by differences in dielectric constants between the two fluids. Like conventional DEP, the surface charge density and the resulting interfacial force have high and low frequency asymptotes values and is determined by taking the appropriate limits of Equation 31. As shown in figure 12, for the low frequency regime, the limiting value is obtained by evaluating $K(\omega \rightarrow 0)$ and is expressed as $\frac{\Delta\sigma}{\sigma_1+\sigma_2}$, while the high frequency asymptote is obtained by evaluating $K(\omega \rightarrow \infty)$ and is expressed as $\frac{\Delta\varepsilon}{\varepsilon_1+\varepsilon_2}$.

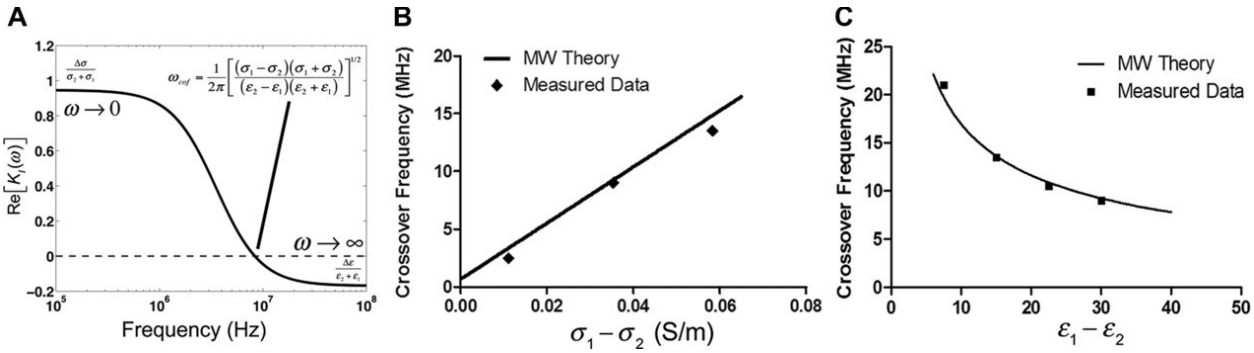

Figure 12. (A) A plot of the real part of the interfacial polarization factor as a function of electric field frequency. The low frequency limit is dictated by the liquid electric conductivity differences. The cross-over frequency is the frequency at which the polarization factor equals zero and is given by equation 30. The high frequency limit is dependent on the differences of electrical permittivity. (B) The cross-over frequency increases linearly with differences in electrical conductivity and shows a good agreement with equation 30. (C) The cross-over frequency decreases with increasing permittivity mismatch. The polarization theory and measured data points show good agreement[6].

Since the electrical force is proportional to the sign and magnitude of the induced surface charge, the two fluids have an interfacial deflection that scales with Equation 31. For fluids with

mismatched electrical properties, such as AHA and PBS, we observed deflection of the high dielectric fluid into the high conductivity fluid at frequencies above the COF of 7.6 MHZ, whereas the high conductive fluid deflected into the high dielectric fluid at low frequencies. Further, for the DB fluids with equal dielectric constants and disparaging conductivities, the fluids behavior is explained by the low frequency regime and the driving force is the difference in conductivities of the two co-flowing fluids. For these fluids, there is no observed COF for all frequencies (1-20 MHz) since the theoretical COF is well above these frequencies.

4.2 Design Variations

In the design of our MEMS, we varied parameters such as electrode separation, the height of the SU-8 polymer mold, the geometries of both the PDMS flow layer and the thin film electrode design. Our experiments indicated that decreasing the spacing between the electrodes resulted in a larger percentage of fluid displacement at the junction. The interdigitated electrodes are more easily aligned by eye, whereas the teeth array require alignment under an inverted microscope. Since the PDMS shrinks in the oven, which can affect the alignment, we used the interdigitated electrode array to mitigate misalignment. The alignment of the electrode array is essential for fabricating microchips that can precisely change the direction of the chemical gradient in the connecting channels.

Although the interdigitated and teeth thin-film both serve as deflection electrodes, the use of the interdigitated electrodes increased the interfacial deflection at the same electrode separation as the teeth electrodes. This is partially due to the increased surface area of the electrodes and the co-flowing fluids. Further, the use of the interdigitated electrode array has both advantages and drawbacks. However, a drawback of this design for chemotaxis assays was an increase in bubble generation and faradaic reactions that produce gases in the microchip (Figure 13).

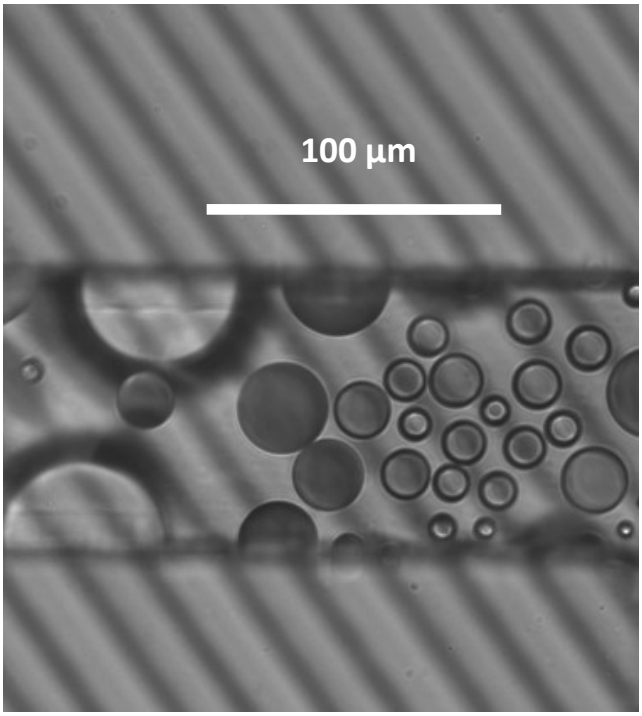

Figure 13. Bubble generation due to faradaic reactions from the interdigitated electrode array.

4.3 Variation in Junction Type

As mentioned earlier, we characterized the deflection in three distinct junctions—y, L and Y. As shown in figure 14, we present three different flow layers that were used to characterize the amount of fluid deflected at the junction located at the end of the electrode array. However, we utilized a y-junction, as it exhibits the promise in the control of fluid deflection. Namely, there was a large range of deflection, as well as demonstrating a frequency dependency that can be exploited for precise delivery of concentration gradients.

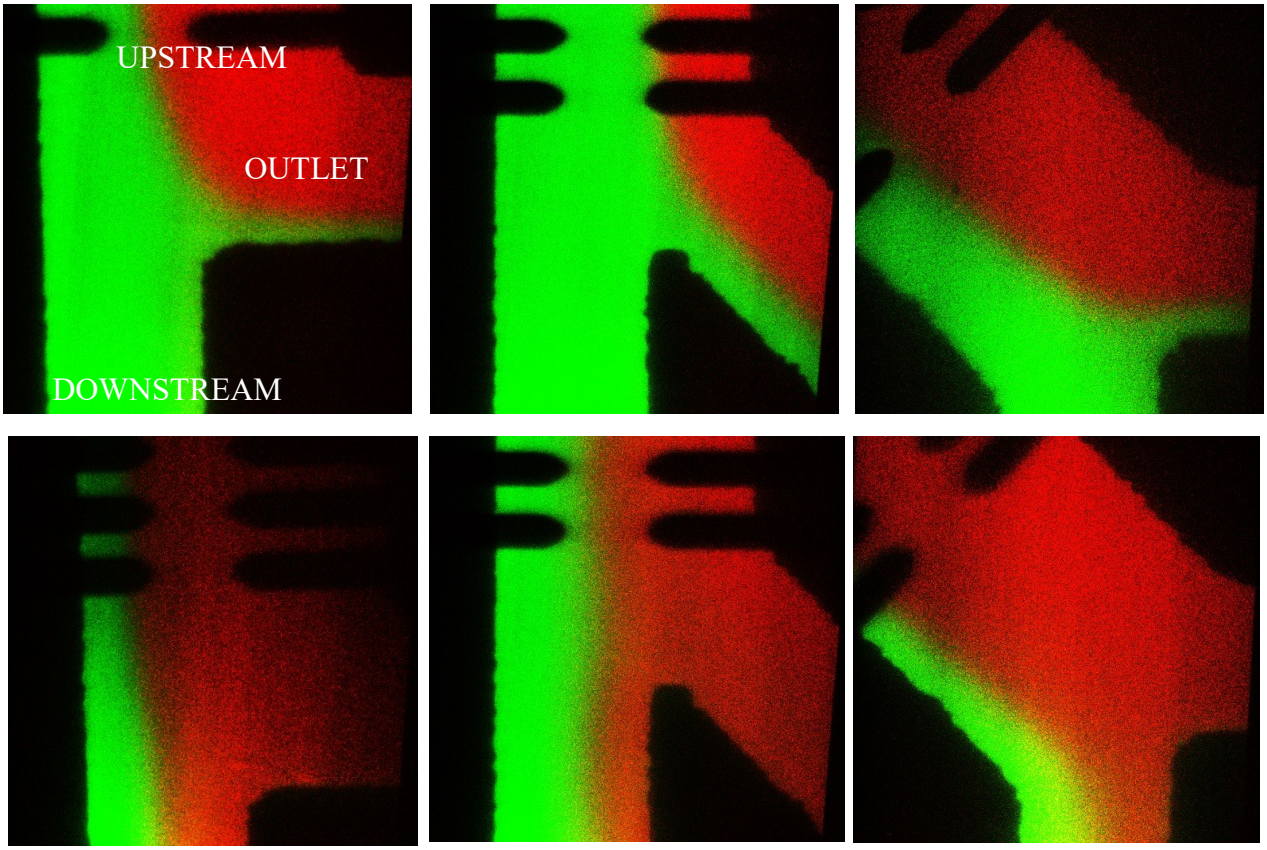

Figure 14. Confocal images of the microfluidic junctions that were used for deflection characterization. The top row is images of the junction when there is not electric field applied, whereas, the bottom row of images is of the junction where an electric field of 20 MHz and 20 V_{pp} is applied and deflection is driven by positive dielectrophoresis.

4.4 Height Variation

We conducted fluidic characterization experiments with microchips of varying height (25 and 50μm). As the flowrate in the microfluidic channel varies drastically with microchannel height and nearly linear with height to width ratio, it was no surprise that changing the height would impact interfacial deflection. As the electric field decays exponentially at increasing

heights above the coplanar electrode surface of the MEMS, most of the deflection occurs at the surface demonstrating a frequency behavior. In the system demonstrated in figure 15, the COF is 7.6MHz and there is frequency dependent behavior that can be observed. Namely, at frequencies below the COF the high conductive fluid displaces on the surface of the MEMS and thus the high dielectric fluid is sent downstream at the top of the microchannel. Contrastingly, at frequencies above the COF the high dielectric stream is displaced into the high conductive stream and is driven down stream on the surface of the MEMS.

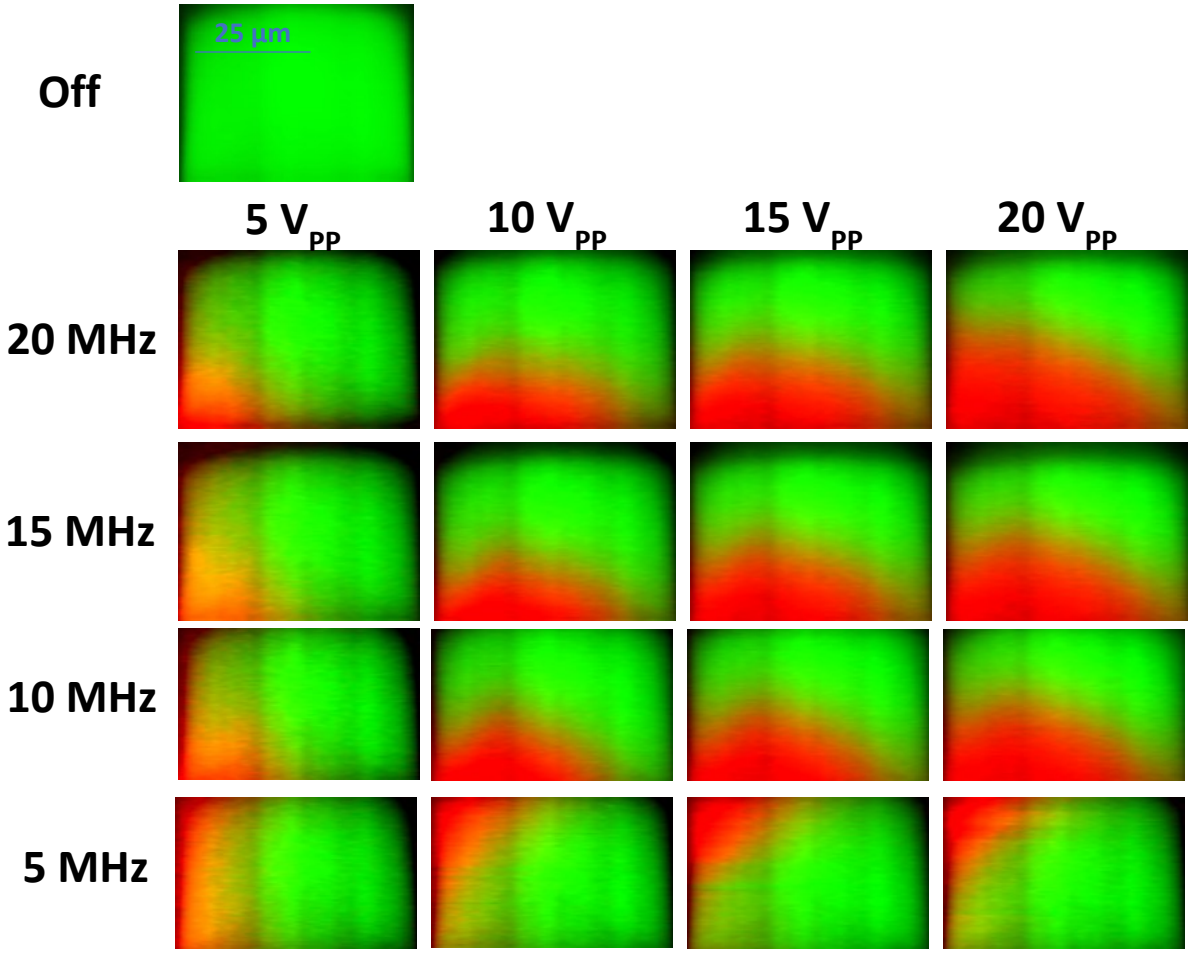

Figure 15. Panel of cross-section images from the Y-junction with a channel height of 50 µm.

In contrast to utilizing microchips with a height of 50µm, devices with a height of 25µm demonstrated a cross section that exhibited a linear interface between the streams (Figure 16). This was an interesting observation because it enables easy quantification of the amount of fluid deflection without an advanced MATLAB method.

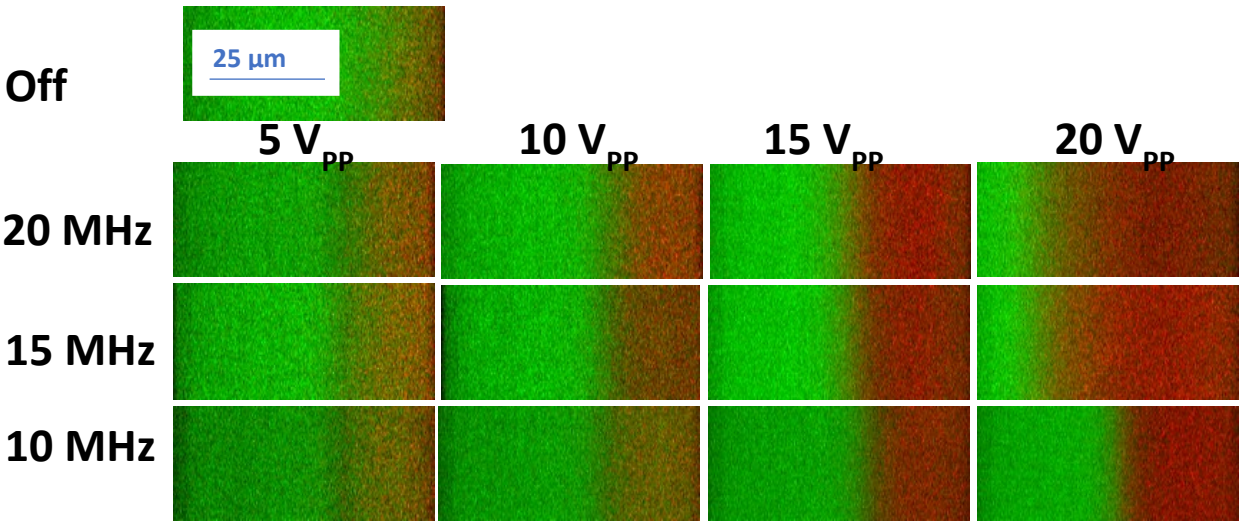

Figure 16. Panel of cross-section images from the y-junction with a channel height of 25 µm.

As seen in figure 17, we determined that the Y-junction resulted in a 2-fold increase in the magnitude of the deflection compared to the L-junction.

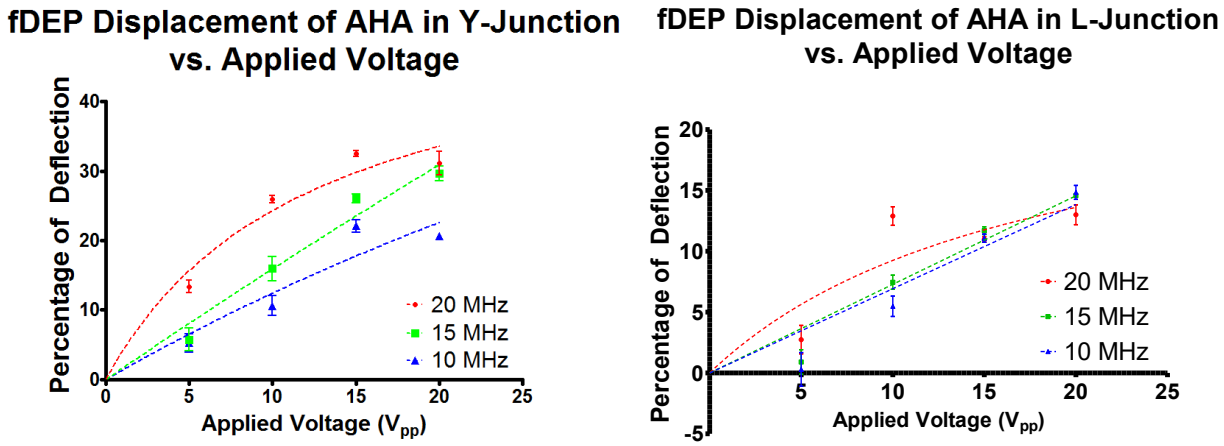

Figure 17. Deflection measurements for the Y and L junctions.

4.5 Measurements for Varying Inlet Pressures

After narrowing down the three flow layers, we decided to do further deflection measurements for the y-junction. We adjust the inlet pressure to low, moderate and high inlet pressures to obtain an outlet flowrate of 0.5, 1.0 and 1.5 µL min^{-1}, respectively. We observed higher deflection for the same applied voltage and frequency for relatively lower inlet pressures. This is partly because the resonance time increases as the inlet pressures decrease and there is more time for the fluid interface to feel the effect of the electric field.

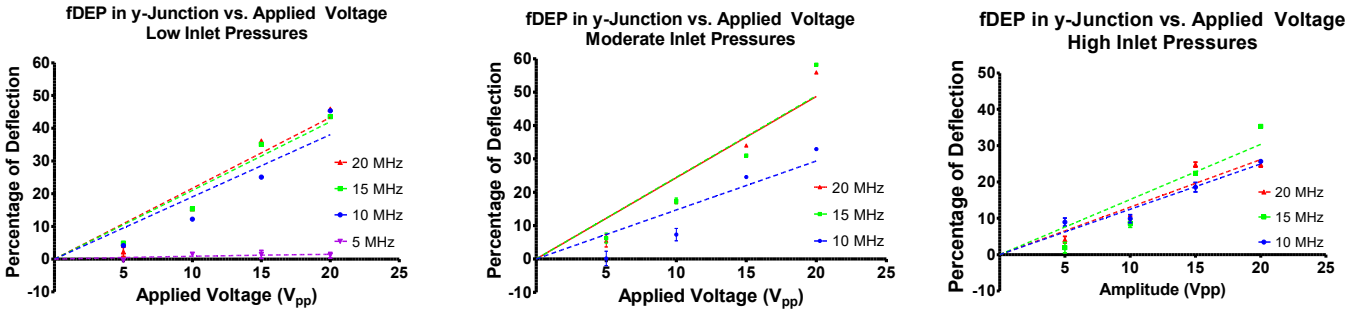

Figure 18. Deflection measurements for the y-junction at varying inlet pressures.

4.6 Measurements of DB Deflection

After determining the optimal flow layer for our applications, we considered different fluids for various biological and medical applications. In this paper, we focus on the application for chemotaxis of *D. discoideum* cells. As mentioned previously, we observed a COF for the PBS and AHA fluid system, as well as a frequency dependent direction of deflection. For the DB fluid system, we observe similar behavior, but due to the large difference in fluid conductivities, the COF is well above the frequencies studied in this paper and thus is not observed.

We applied this fluid routing technology to biologically relevant fluids. We use DB since it is a biological buffer commonly used for *D. discoideum* cell media. By adjusting the concentrations of magnesium and calcium chloride, we developed a low calcium buffer compatible with *D. discoideum* cells. The two DB fluids had equal dielectric constants but disparaging conductivities. Thus, we used the low frequency regime of the polarization factor to describe the fluid deflection. We conducted similar measurements to the control fluids, AHA and PBS, by utilizing our custom MATLAB method to quantify the amount of deflection at the junction and have demonstrated the results in figure 19.

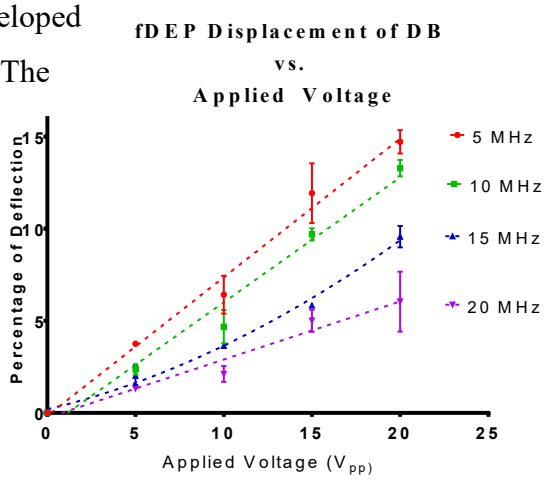

Figure 19. Deflection measurements of positive fluidic dielectrophoresis for developmental buffer and developmental buffer with a relatively lower conductivity. (Three images were acquired for measurements at each condition.)

Chapter 5

Conclusion and Future Work

This paper demonstrates the ability to precisely route fluids based on an electrokinetic phenomena and intrinsic fluid properties. The symmetrical nature of our technology serves as platform to establish chemical gradients that can act as a switch for chemical signaling. This switch offers an ability to robustly control both the direction and the magnitude of chemical signals. Although the deflection does not reach equilibrium instantaneously, it is reached in microseconds and thus it is a highly advantageous tool for biological applications that require robust control of chemical gradients under short timescales.

Our device is noteworthy for its ease and ability to induce precise fluid motion based on an intrinsic property, such as differences in polarizabilities. By exploiting AC electrokinetics, we take advantage of the frequency dependent behavior of the CM factor for defined on chip fluid-routing.

A plethora of electrode geometries can be included to enhance the electronic capability of our device. Specifically, as seen in figure 17, an additional electrode array was fabricated downstream the microfluidic junction to incorporate an active mixer to deliver uniform concentration gradients. Future work will characterize the degree of mixing of this additional electrode array. Similarly, by incorporating impedance sensors and developing a circuit model, we can non-optically measure interfacial COF and downstream concentrations.

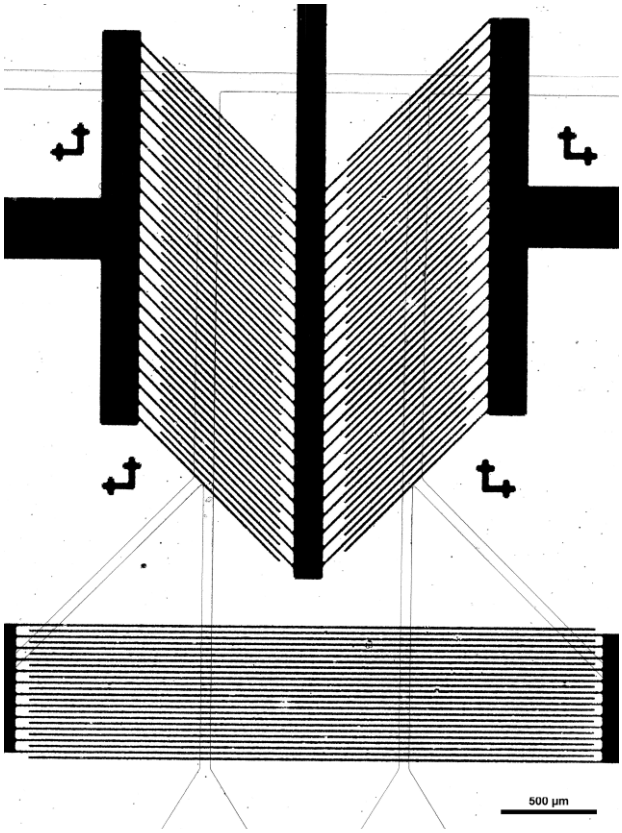

Figure 20. Brightfield image of a MEMS with interdigitated electrodes upstream the y-junction, as well as, interdigitated electrodes downstream the junction for mixing.

Image acquisition with fluorescent tracers and confocal microscopy have certain limitations in the context of chemotaxis studies. Although confocal microscopy can

capture three-dimensional images, the excitation light produced by the solid-state laser affect the morphology of cells. When exposed to the laser for long periods of time, *D. discoideum* cells form spherical structures and do not migrate. Consequently, confocal microscopy using solid-state lasers cannot be used for extending imaging, which is often required for biological analysis. Although fluorescents are a widely-used tool in biological and medical research, they are not photostable and undergo photobleaching.

One future consideration to overcome these limitations is to incorporate quantum dots, more commonly known as semiconducting nanocrystals, as an imaging technique to mitigate laser exposure. Nanocrystals have tunable, symmetric emission spectrum and are photochemically stable and have to potential to replace fluorescence, a widely used tool in biology[13]. The use of quantum dots will be employed to image chemical uptake and actin reorganization at a single excitation wavelength. In addition to structural reorganization, we hope to use such imaging techniques to research the specific pathways involved for chemical molecules in receptor mediated transport. Further considerations will include characterizing different modes of cell motility using DNA recombinant techniques to knock out specific protein functions. Transfection of *D. discoideum* cells or standard mutagenesis techniques can be employed to research the effects of mutant cell motility and shed light on cell locomotion.

In short, we have developed a platform for on-chip fluid routing with the purpose of actuating chemical gradients in microenvironments. Our technology demonstrates the ability to modulate both the direction and magnitude of chemical of gradients in short timescales for biologic and medical applications such as cellular chemotaxis. We employed fluidic dielectrophoresis (fDEP) as a method to fabricate a fluid routing device capable of tuning spatial chemical gradients under short timescales. Our device enables control of chemical gradient to research directional sensing, cellular motility and morphology.

References

1. Pohl, H. A., Pollock, K. & Crane, J. S. Dielectrophoretic force: A comparison of theory and experiment. *Journal of Biological Physics* **6,** 133–160 (1978).
2. Sackmann, E. K., Fulton, A. L. & Beebe, D. J. The present and future role of microfluidics in biomedical research. *Nature* **507,** 181–189 (2014).
3. Dertinger, S. K. W., Chiu, D. T., Noo Li Jeon & Whitesides, G. M. Generation of gradients having complex shapes using microfluidic networks. *Analytical Chemistry* **73,** 1240–1246 (2001).
4. Raja, W. K., Gligorijevic, B., Wyckoff, J., Condeelis, J. S. & Castracane, J. A new chemotaxis device for cell migration studies. *Integrative Biology* **2,** 696 (2010).
5. Ebrahimzadeh, P. R., Hogfors, C. & Braide, M. Neutrophil chemotaxis in moving gradients of fMLP. *Journal of Leukocyte Biology* **67,** 651–661 (2000).
6. Kohidai, L. & Csaba, G. Chemotaxis and chemotactic selection induced with cytokines (IL-8, RANTES and TNF-α) in the unicellular Tetrahymena pyriformis. *Cytokine* **10,** 481–486 (1998).
7. Whitesides, G. M., Ostuni, E., Takayama, S., Jiang, X. & Ingber, D. E. Soft lithography in biology and biochemistry. *Annual review of biomedical engineering* **3,** 335–73 (2001).
8. Desmond, M., Mavrogiannis, N. & Gagnon, Z. Maxwell-Wagner polarization and frequency-dependent injection at aqueous electrical interfaces. *Physical Review Letters* **109,** (2012).
9. Franca-Koh, J., Kamimura, Y. & Devreotes, P. Navigating signaling networks: chemotaxis in Dictyostelium discoideum. *Current Opinion in Genetics and Development* **16,** 333–338 (2006).
10. Ibo, M., Srivastava, V., Robinson, D. N. & Gagnon, Z. R. Cell blebbing in confined microfluidic environments. *PLoS ONE* **11,** (2016).
11. Elveflow Plug and Play Microfluidics. *Microfluidic Flow Controller.* Retreived from https://www.elveflow.com/microfluidic-flow-control-products/flow-control-system/pressure-controller/
12. Rigol. *DG4102 | 100 MHz Arbitrary Waveform Generator*. Retrieved from http://www.rigolna.com/products/waveform-generators/dg4102/
13. Morgan, H. and Green, N.G. (2003) AC electrokinetics: colloids and nanoparticles. Series: Microtechnologies and microsystems series. Research Studies Press: Philadelphia, PA, USA. ISBN 9780863802553
14. Bruchez, M., Moronne, M., Gin, P., Weiss, S. & Alivisatos, A. P. Semiconductor nanocrystals as fluorescent biological labels. *Science* **281,** 2013–2016 (1998).
15. Ramos, A., Morgan, H., Green, N. G. & Castellanos, A. Ac electrokinetics: A review of forces in microelectrode structures. *Journal of Physics D: Applied Physics***31,**2338–2353 (1998).
16. Pergolizzi, B., Bozzaro, S. & Bracco, E. G-protein dependent signal transduction and ubiquitination in dictyostelium. *International Journal of Molecular Sciences* **18,** (2017).

Edwin David Lavi

edwlavi@gmail.com, +1 (516) 477 2621

Education

Johns Hopkins University — **Baltimore, MD**

M.S. Chemical & Biomolecular Engineering — Expected May 2018

B.S. Chemical & Biomolecular Engineering — May 2017

- Molecular and Cellular Bioengineering Track

Selected Coursework: Transport Phenomena, Electrokinetics, Dielectrophoresis, Microfluidics, Process Dynamics and Control, Directed Evolution, Systems Pharmacology and Personalized Medicine, Computational Design and Structure of Proteins

Professional Experience

Gagnon Microfluidics Laboratory, Johns Hopkins University — **Baltimore, MD**

Electrokinetic and Microfluidic Researcher — September 2016 – current

- Designed microfluidic devices in a class 100 clean room to investigate cellular modes of motility and chemotactic speed/velocity in response to varying chemoattractant concentration gradients and steepness
- Utilized a Nikon Confocal microscope and the accompanying NIS Elements software to capture and analyze fluidic dielectrophoresis that drives the concentration gradients to anaerobes in confinement
- Chemically deposited chromium and gold onto glass fabricating electrodes on a 2D glass surface for bonding of PDMS to displace co-flowing fluids of mismatched conductivities and dielectric constants
- Developed a MATLAB method to segment images to determine downstream concentration

Sean X. Sun Laboratory, Johns Hopkins University — **Baltimore, MD**

Micro-fabrication and Cell Biology Research Assistant — June 2015 – September 2016

- Undergraduate Lab Captain accountable for undergraduate lab member responsibilities
- Developed soft and hard photolithographic procedures, produced silicon molds with micrometer precision and fabricated PDMS microfluidics devices for a study of single cell dynamics
- Wrote MATLAB methods and processed time-lapse images of fluorescent tagged cells exposed to an external force within a microfluidic device for cell volume analysis
- Designed and manufactured a custom anaerobic chamber, water bath and bioreactor to quantify the bio-hydrogen production of a thermophilic and anaerobic microorganism
- Designed an attachment for a centrifuge in CAD for compatibility of cells in microfluidic device and manufactured it using a 3D printer and conducted stress and deformation calculations on the model

Leadership Experience

Teaching Assistant — **Baltimore, MD**

Dynamic Modeling and Control of Chemical and Biological Systems — August 2017 – January 2018

Transport Phenomena — January 2018 – May 2018

- Responsibilities included conducting 3 sessions a week to review course material, grading homework assignments, overseeing lab sessions and proctoring exams.

Product Design — **Baltimore, MD**

Team Leader — September 2016 – Present

- Manufactured a nano-porous Gold vehicle as a wearable jewelry for controlled release of volatile solutions that were modeled with pervaporation phenomena for mixtures

Undergraduate Senior Chemical Engineering Lab — **Baltimore, MD**

Membrane Separation, Bioreactor and Biocatalysis Engineer — October 2017 – May 2018

- Conducted a pilot operation and determined the optimal conditions for separation of Rhodamine B from Dextran FITC and a conducted a scale-up analysis of the ultrafiltration process
- Optimized the fermentation conditions for E. Coli strain WM04 for use in a Bacteria Directed Enzyme Prodrug Therapy to target tumor sites upon injection in the human body
- Optimized an enzymatic reaction to produce a chemical with anti-tumor activity

Institute for NanoBioTechnology Undergraduate Leadership Committee **Baltimore, MD**

Lab Leader October 2014 – May 2018

- Organized an annual Undergraduate Research Symposium for INBT students to showcase research to receive feedback from faculty member and established organizations in NanoBioTechnology

Technical Skills

Lab: Bioreactor Design, Cell Culture, PCR, Fluorescent Imaging, Soft and Hard Photolithography, CD Spectroscopy, Native-PAGE, Agarose Gel Electrophoresis, Chromatography, Metal De-alloying, NIS Elements
Programming: Python, Matlab, PyRosetta, R, LaTex, 3D Modeling, Monte Carlo, PyMol, ASPEN, AutoCAD